Testing neutrino electromagnetic properties at current and future dark matter experiments

Carlo Giunti[1,*] and Christoph A. Ternes[2,†]

[1]*Istituto Nazionale di Fisica Nucleare (INFN), Sezione di Torino, Via P. Giuria 1, I–10125 Torino, Italy*
[2]*Istituto Nazionale di Fisica Nucleare (INFN), Laboratori Nazionali del Gran Sasso, 67100 Assergi, L'Aquila, Italy*

(Received 11 October 2023; accepted 7 November 2023; published 27 November 2023)

We analyze data from the dark matter direct detection experiments PandaX-4T, LUX-ZEPLIN and XENONnT to place bounds on neutrino electromagnetic properties (magnetic moments, millicharges, and charge radii). We also show how these bounds will improve at the future facility DARWIN. In our analyses we implement a more conservative treatment of background uncertainties than usually done in the literature. From the combined analysis of all three experiments we can place very strong bounds on the neutrino magnetic moments and on the neutrino millicharges. We show that even though the bounds on the neutrino charge radii are not very strong from the analysis of current data, DARWIN could provide the first measurement of the electron neutrino charge radius, in agreement with the Standard Model prediction.

DOI: 10.1103/PhysRevD.108.095044

I. INTRODUCTION

The investigation of neutrino properties is one of the most active research fields in particle physics. In the Standard Model neutrinos are massless particles which interact only via weak interactions. Through the observation of neutrino oscillations we know, however, that at least two neutrinos are massive particles. Therefore, the Standard Model has to be extended to account for neutrino masses.

In some of the extensions of the Standard Model neutrinos can acquire electromagnetic properties through quantum loop effects. Therefore, some models of physics beyond the Standard Model predict the interaction of neutrinos with electromagnetic fields and electromagnetic interactions with charged particles. Moreover, even the Standard Model predicts nonzero neutrino charge radii due to radiative corrections. For detailed reviews on the theories of neutrino electromagnetic properties we refer the reader to Refs. [1,2].

In this paper we test the neutrino electromagnetic properties (magnetic moments, millicharges, and charge radii) by analyzing data from dark matter direct detection experiments. These experiments aim to measure the nuclear or electron recoils from dark matter interacting with the material in the detector, which is xenon for all experiments under consideration in this work. In this paper we consider the data from the PandaX-4T experiment [3], from LUX-ZEPLIN (LZ) [4], and from XENONnT [5]. We also show the sensitivity of the future experiment DARWIN [6].

One of the background sources for the dark matter search in these experiments is the elastic scattering of solar neutrinos on the electrons in the detector material. Therefore, if some new physics model changes the standard electron-neutrino elastic scattering (EνES) cross section, it can be tested at dark matter direct detection experiments. One possibility to alter this process is the presence of neutrino electromagnetic properties.

Our paper is structured as follows: In Sec. II we discuss how neutrino magnetic moments, neutrino millicharges and neutrino charge radii alter the EνES process. In Sec. III we detail the analysis procedure of the experiments under consideration. We proceed to present and discuss our results in Sec. IV, before concluding in Sec. V.

II. THEORETICAL FRAMEWORK

In this paper we obtain bounds on neutrino electromagnetic properties from the data of Xenon dark matter experiments through the elastic scattering of solar neutrinos with electrons (EνES). These experiments are sensitive to the neutrino electromagnetic properties through their contributions to EνES in addition to the Standard Model EνES cross section. Therefore, we first present the Standard Model EνES cross section in Sec. II A, and then we discuss the cross sections due to the neutrino electromagnetic properties that we consider; magnetic moments in

*carlo.giunti@to.infn.it
†christoph.ternes@lngs.infn.it

Sec. II B, electric charges in Sec. II C, and charge radii in Sec. II D. These three electromagnetic properties are the observable effective electromagnetic properties of ultrarelativistic neutrinos, for which the effective magnetic moments include possible electric moments and the effective charge radii include possible anapole moments [1,2,7].

Solar neutrinos oscillate and arrive at a detector on Earth as a mixture of ν_e, ν_μ, and ν_τ, whose fluxes are given by

$$\Phi^i_{\nu_e} = \Phi^{i\odot}_{\nu_e} P_{ee}, \qquad \Phi^i_{\nu_\mu} = \Phi^{i\odot}_{\nu_e}(1 - P_{ee})\cos^2\vartheta_{23},$$
$$\Phi^i_{\nu_\tau} = \Phi^{i\odot}_{\nu_e}(1 - P_{ee})\sin^2\vartheta_{23}, \tag{1}$$

where $\Phi^{i\odot}_{\nu_e}$ are the fluxes of ν_e produced by thermonuclear reactions in the center of the Sun, with $i = pp$, ^{7}Be, etc., and P_{ee} is the survival probability of ν_e at the Earth. In our analysis we use the solar spectra taken from Refs. [8–11] using the normalizations for the high metallicity model taken from the review in Ref. [12]. We consider pp and ^{7}Be neutrinos, which give the main contribution to the event rates of the experiments under consideration. For these low-energy solar neutrinos

$$P_{ee} \simeq \left(1 - \frac{1}{2}\sin^2 2\vartheta_{12}\right)\cos^4\vartheta_{13} + \sin^4\vartheta_{13}. \tag{2}$$

Using $\sin^2\vartheta_{12} = 0.318 \pm 0.016$ and $\sin^2\vartheta_{13}|_{\rm NO} = 0.02200^{+0.00069}_{-0.00062}$ or $\sin^2\vartheta_{13}|_{\rm IO} = 0.02225^{+0.00064}_{-0.00070}$ obtained in the global fit of Ref. [13] (see also the similar results obtained in Refs. [14,15]) in the case of normal ordering and inverted ordering of the neutrino masses, we obtain $P_{ee} = 0.542 \pm 0.011$. The fluxes of ν_μ and ν_τ depend on the mixing angle ϑ_{23}, which is close to maximal mixing ($\vartheta_{23} = \pi/4$) [13–15]. For simplicity, we consider $\sin^2\vartheta_{23} = 0.5$, which implies $\Phi^i_{\nu_\mu} = \Phi^i_{\nu_\tau}$. Therefore, we obtain equal constraints on the electromagnetic properties of ν_μ and ν_τ.

A. The Standard Model EνES cross section

The Standard Model EνES cross section per xenon atom is given by

$$\frac{d\sigma^{\rm SM}_{\nu_\ell-{\rm Xe}}}{dT_{\rm e}}(E_\nu, T_{\rm e}) = Z^{\rm Xe}_{\rm eff}(T_e)\frac{G_{\rm F}^2 m_e}{2\pi}\left[(g_V^{\nu_\ell} + g_A^{\nu_\ell})^2 + (g_V^{\nu_\ell} - g_A^{\nu_\ell})^2\left(1 - \frac{T_e}{E_\nu}\right)^2 - ((g_V^{\nu_\ell})^2 - (g_A^{\nu_\ell})^2)\frac{m_e T_e}{E_\nu^2}\right], \tag{3}$$

where $G_{\rm F}$ is the Fermi constant, m_e is the electron mass, E_ν is the neutrino energy, and T_e is the observable electron recoil energy. The neutrino-electron couplings $g^{\nu_\ell}_{V,A}$ depend on the neutrino flavor,

$$g_V^{\nu_e} = 2\sin^2\vartheta_W + 1/2, \qquad g_A^{\nu_e} = 1/2, \tag{4}$$

$$g_V^{\nu_{\mu,\tau}} = 2\sin^2\vartheta_W - 1/2, \qquad g_A^{\nu_{\mu,\tau}} = -1/2, \tag{5}$$

with $\sin^2\vartheta_W = 0.23863 \pm 0.00005$ [16]. The coefficient $Z^{\rm Xe}_{\rm eff}(T_e)$ quantifies the effective number of electrons which can be ionized at T_e [17]. We calculate $Z^{\rm Xe}_{\rm eff}(T_e)$ using Table II of Ref. [18].

B. Neutrino magnetic moments

Neutrino magnetic moments are predicted by many theories with massive neutrinos beyond the Standard Model (BSM) and have been constrained by many observations (see, e.g., Refs. [1,2,7,16]). The most stringent experimental limit $|\mu_{\nu_e}| < 2.9 \times 10^{-11}\mu_B$ at 90% C.L., where μ_B is the Bohr magneton, was obtained in the GEMMA experiment [19] through the EνES of reactor $\bar\nu_e$. This bound is more than eight orders of magnitude larger than the prediction of neutrino magnetic moments in the minimal extension of the SM with right handed neutrinos and Dirac neutrino masses [20–22]. However, in more elaborate models (see, e.g., the review in Ref. [1]), the neutrino magnetic moments can be larger and can be probed in current experiments.

The contribution of the neutrino magnetic moments to EνES is incoherent with the Standard Model contribution because the neutrino magnetic moment interaction flips the helicity of ultrarelativistic neutrinos, whereas the Standard Model weak interaction is helicity conserving. Therefore, for each flavor neutrino ν_ℓ the total cross section is given by the sum of the Standard Model cross section (3) and the magnetic moment cross section

$$\frac{d\sigma^{\rm MM}_{\nu_\ell-{\rm Xe}}}{dT_{\rm e}}E(E_\nu, T_{\rm e}) = Z^{\rm Xe}_{\rm eff}(T_{\rm e})\frac{\pi\alpha^2}{m_e^2}\left(\frac{1}{T_{\rm e}} - \frac{1}{E_\nu}\right)\left|\frac{\mu_{\nu_\ell}}{\mu_{\rm B}}\right|^2, \tag{6}$$

where α is the fine-structure constant. For the low values of $T_{\rm e}$ in the experiments under consideration ($T_{\rm e} \lesssim 30$ keV), the cross section (6) is approximately proportional to $T_{\rm e}^{-1}$. Therefore, the effects of the neutrino magnetic moments are probed by the observation of an event excess near the $T_{\rm e}$ threshold.

C. Neutrino electric charges

In the Standard Model neutrinos are neutral, but in BSM theories they can have small electric charges, often called "millicharges" (see, e.g., the review in Ref. [1]), which can

be probed in neutrino scattering experiments. In general, the three flavor neutrinos can have the millicharges q_{ν_e}, q_{ν_μ}, and q_{ν_τ}, and there can be also the three transition electric charges $q_{\nu_{e\mu}}$, $q_{\nu_{e\tau}}$, and $q_{\nu_{\mu\tau}}$.

Since the electric charge interaction conserves the helicity of ultrarelativistic neutrinos and the millicharges of the flavor neutrinos conserve the neutrino flavor, they contribute coherently with the Standard Model interaction, which is helicity and flavor conserving. On the other hand, since the transition electric charges induce a change of flavor they contribute incoherently with the Standard Model interaction. Therefore, the total EνES cross section is given by

$$\frac{d\sigma^{\rm SM+EC}_{\nu_\ell-{\rm Xe}}}{dT_{\rm e}} = \left(\frac{d\sigma^{\rm SM+EC}_{\nu_\ell-{\rm Xe}}}{dT_{\rm e}}\right)_{q_{\nu_\ell}} + \sum_{\ell'\neq\ell}\left(\frac{d\sigma^{\rm EC}_{\nu_\ell-{\rm Xe}}}{dT_{\rm e}}\right)_{q_{\nu_{\ell\ell'}}}, \quad (7)$$

where $(d\sigma^{\rm SM+EC}_{\nu_\ell-{\rm Xe}}/dT_{\rm e})_{q_{\nu_\ell}}$ is given by Eq. (3) with

$$g_V^{\nu_\ell} \to g_V^{\nu_\ell} - \frac{\sqrt{2}\pi\alpha}{G_{\rm F} m_e T_e} q_{\nu_\ell}, \quad (8)$$

and

$$\left(\frac{d\sigma^{\rm EC}_{\nu_\ell-{\rm Xe}}}{dT_{\rm e}}\right)_{q_{\nu_{\ell\ell'}}} = Z^{\rm Xe}_{\rm eff}(T_e)\frac{\pi\alpha^2}{m_e T_{\rm e}^2}\left[1+\left(1-\frac{T_{\rm e}}{E_\nu}\right)^2 - \frac{m_e T_{\rm e}}{E_\nu^2}\right] \times |q_{\nu_{\ell\ell'}}|^2, \quad (9)$$

for $\ell' \neq \ell$. Hence, EνES gives full information on the charges q_{ν_ℓ} of the flavor neutrinos, including their sign, whereas only the absolute values of the transition electric charges $q_{\nu_{\ell\ell'}}$ can be probed. Note also that the effects of the electric charges are enhanced at small values of T_e, leading to the possibility to probe very small electric charges in low-threshold experiments.

D. Neutrino charge radii

Even if neutrinos are neutral, they can have charge radii. Indeed, even in the Standard Model the massless and neutral flavor neutrinos have tiny charge radii induced by radiative corrections, which are given by [23–25] (with the definition of the charge radii in Refs. [26,27])

$$\langle r^2_{\nu_\ell}\rangle_{\rm SM} = -\frac{G_{\rm F}}{2\sqrt{2}\pi^2}\left[3 - 2\ln\left(\frac{m_\ell^2}{m_W^2}\right)\right], \quad (10)$$

where m_W and m_ℓ are, respectively, the W boson and charged lepton masses ($\ell = e, \mu, \tau$). Numerically, we have

$$\langle r^2_{\nu_e}\rangle_{\rm SM} = -0.83 \times 10^{-32}\ {\rm cm}^2, \quad (11)$$

$$\langle r^2_{\nu_\mu}\rangle_{\rm SM} = -0.48 \times 10^{-32}\ {\rm cm}^2, \quad (12)$$

$$\langle r^2_{\nu_\tau}\rangle_{\rm SM} = -0.30 \times 10^{-32}\ {\rm cm}^2. \quad (13)$$

These diagonal charge radii of the flavor neutrinos are the only charge radii that exist in the Standard Model, where neutrino flavor is conserved.

In BSM theories neutrinos can have also the transition charge radii $\langle r^2_{\nu_{e\mu}}\rangle$, $\langle r^2_{\nu_{e\tau}}\rangle$, and $\langle r^2_{\nu_{\mu\tau}}\rangle$ which induce flavor transitions in scattering processes. We consider the general case with both diagonal and transition charge radii. As for the electric charges discussed in Sec. II C, the diagonal charge radii contribute to the EνES cross section coherently with the Standard Model interaction, because both conserve the helicity of ultrarelativistic neutrinos and neutrino flavors, whereas the transition charge radii contribute incoherently. Therefore, the total EνES cross section is given by

$$\frac{d\sigma^{\rm SM+CR}_{\nu_\ell-{\rm Xe}}}{dT_{\rm e}} = \left(\frac{d\sigma^{\rm SM+CR}_{\nu_\ell-{\rm Xe}}}{dT_{\rm e}}\right)_{\langle r^2_{\nu_\ell}\rangle} + \sum_{\ell'\neq\ell}\left(\frac{d\sigma^{\rm CR}_{\nu_\ell-{\rm Xe}}}{dT_{\rm e}}\right)_{\langle r^2_{\nu_{\ell\ell'}}\rangle}, \quad (14)$$

where $(d\sigma^{\rm SM+CR}_{\nu_\ell-{\rm Xe}}/dT_{\rm e})_{\langle r^2_{\nu_\ell}\rangle}$ is given by Eq. (3) with

$$g_V^{\nu_\ell} \to g_V^{\nu_\ell} + \frac{\sqrt{2}\pi\alpha}{3G_{\rm F}}\langle r^2_{\nu_{\ell\ell'}}\rangle, \quad (15)$$

and

$$\left(\frac{d\sigma^{\rm CR}_{\nu_\ell-{\rm Xe}}}{dT_{\rm e}}\right)_{\langle r^2_{\nu_{\ell\ell'}}\rangle} = Z^A_{\rm eff}(T_e)\frac{\pi\alpha^2 m_e}{9}\left[1+\left(1-\frac{T_e}{E_\nu}\right)^2 - \frac{m_e T_e}{E_\nu^2}\right] \times |\langle r^2_{\nu_{\ell\ell'}}\rangle|^2, \quad (16)$$

for $\ell' \neq \ell$. As for the electric charges discussed in Sec. II C, EνES gives full information on the diagonal charge radii $\langle r^2_{\nu_\ell}\rangle$ of the flavor neutrinos, including their sign, and only information on the absolute values of the transition electric charges $\langle r^2_{\nu_{\ell\ell'}}\rangle$.

III. DATA ANALYSIS

A. Current experiments

In the analyses presented in this paper we include data from LZ [4], XENONnT [5] and PandaX-4T [3]. In this section we discuss the details of each analysis. For an experiment X the overall predicted number of events in a given energy-bin k is given by

$$R_k^X = R_k^{E\nu ES} + \sum_i R_k^i, \quad (17)$$

where $R_k^{E\nu ES}$ is the contribution from solar neutrinos which elastically scatter on electrons, while R_k^i are the remaining background components. We have extracted the

contributions R_k^i for the different experiments from Refs. [3,5,28] and $R_k^{E\nu ES}$ is obtained from

$$R_k^{E\nu ES} = N \int_{T_e^k}^{T_e^{k+1}} dT_e \int_0^\infty dT'_e R(T_e, T'_e) A(T'_e) \times \sum_{i=pp,{}^7\mathrm{Be}} \int_{E_\nu^{\min}}^{E_{\nu,i}^{\max}} dE_\nu \sum_\ell \Phi^i_{\nu_\ell}(E_\nu) \frac{d\sigma_{\nu_\ell}}{dT'_e}. \quad (18)$$

In this expression T_e and T'_e are the reconstructed and true electron recoil energies, while E_ν is the neutrino energy. The electron-neutrino cross section for a given neutrino flavor ν_ℓ is given by $d\sigma_{\nu_\ell}/dT'_e$ and $\Phi^i_{\nu_\ell}(E_\nu)$ are the solar neutrino fluxes from Eq. (1). The minimal neutrino energy to produce an electron recoil of T'_e is given by $E_\nu^{\min} = (T'_e + \sqrt{2m_e T'_e + T'^2_e})/2$, while the maximal neutrino energy $E_{\nu,i}^{\max}$ depends on the production process, indicated with the index i. Next, $R(T_e, T'_e)$ and $A(T'_e)$ are the detector resolution and efficiency and are different for all experiments. Finally, N is a normalization constant which takes into account the exposure and detector volume. Also this quantity is different for each experiment.

For the analysis of the experiments under consideration we use the detector efficiencies from Refs. [3,5,29]. For the energy resolution at LZ we use the same function that has been used in Refs. [18,30]. In the case of XENONnT we use the resolution function of Ref. [31] and for PandaX-4T we use the one from Ref. [3].

The predicted number of events in Eq. (17) has to be compared with the data D^X accumulated in each experiment. We use the data presented in Fig. 6 of Ref. [4] for LZ[1] and the data in Fig. 3 of Ref. [3] for PandaX-4T. For XENONnT we use the data from Fig. 4 (5) of Ref. [5] for recoil energies above (below) 30 keV.

Due to the low statistics in some of the bins, for LZ and PandaX-4T we use the Poissonian least-squares function

$$\chi^2_X = \min_{\vec{\alpha},\vec{\beta}} \left\{ 2\left(\sum_k R_k^X - D_k^X + D_k^X \log D_k^X/R_k^X \right) + \sum_i (\alpha_i/\sigma_{\alpha_i})^2 + \sum_i (\beta_i/\sigma_{\beta_i})^2 \right\}, \quad (19)$$

where α_i are normalization constants multiplied to each single background component in Eq. (17). For LZ, the uncertainties σ_{α_i} are extracted from Ref. [28]. For PandaX-4T, they are taken from Ref. [3]. Note that some of them are left to vary freely in the analysis. Also included are uncertainty coefficients β_i of the solar neutrino fluxes, with uncertainties σ_{β_i} taken from Ref. [12].

[1]We do not use the timing data from Ref. [29], which could result only in a 5% improvement in the bounds.

In the case of XENONnT data, we use instead

$$\chi^2_{\mathrm{XENONnT}} = \min_{\vec{\alpha},\vec{\beta}} \left\{ \sum_k \left(\frac{R_k^{\mathrm{XENONnT}} - D_k^{\mathrm{XENONnT}}}{\sigma_k} \right)^2 + \sum_i (\alpha_i/\sigma_{\alpha_i})^2 + \sum_i (\beta_i/\sigma_{\beta_i})^2 \right\}, \quad (20)$$

where the uncertainties in each bin σ_k are extracted from Ref. [5]. The remaining components are equivalent to the corresponding ones for LZ and PandaX-4T.

We also perform a combined analysis of all three experiments. In this case we correlate the uncertainties regarding the neutrino flux among the experiments. In addition, several of the background components are common to at least two of the three experiments. In these cases we also correlate the normalizations of the background components. While such a combined analysis has not been performed yet, we have noticed that this correlated analysis produces only slightly tighter bounds than simply summing up the individual χ^2.

B. DARWIN sensitivity

We also compute the sensitivity to electromagnetic neutrino properties for the future experiment DARWIN. The calculation of the event rate at DARWIN is basically the same as for the current experiments, given in Eqs. (17) and (18), but we also include the contributions from solar N, O, and *pep* neutrinos. Note, however, that their contribution is mostly negligible in comparison with some of the background contributions, as shown in Fig. 1 of Ref. [6]. We include them, nevertheless, since we use the full spectrum as shown in Ref. [6]. The energy dependence of the neutrino oscillation probability is taken into account for these higher-energy neutrinos.

For the individual background components we use the spectra given in Ref. [6], which need to be normalized to the considered exposure. Due to lack of more detailed information, we use the same resolution function and detector efficiency as for XENONnT. We assume the efficiency to remain constant for $T_e > T_{e,\max}^{\mathrm{XENONnT}}$. With these assumptions, we are able to reproduce the EνES spectra for all five neutrino species in Fig. 1 of Ref. [6], which validates our choice of efficiency and resolution. As was done in Ref. [6], we consider different scenarios for the DARWIN sensitivity. First we assume an exposure of 30 ty. Next, we assume an exposure of 300 ty. Finally, we assume an exposure of 300 ty again, but also that the ^{136}Xe background component is depleted to 1%.

When generating the mock data, always compatible with the Standard Model, we use 51 logarithmically spaced bins between 1 keV and 1500 keV recoil energy. Note that the spectrum at higher energies is not sensitive to any BSM effect considered in this paper, because the EνES rate is much smaller than some of the background rates. We still

use the full spectrum, since the inclusion of events at high energies can help to control the effect of background uncertainties.

IV. RESULTS

In this section we present the bounds that can be obtained from current data and the sensitivity at DARWIN to neutrino electromagnetic properties.

A. Neutrino magnetic moments

We first discuss neutrino magnetic moments. Our results are presented in Fig. 1 and Table I. In the first column of Table I we present the bounds on the magnetic moment μ_{ν_e}. In the second we present the results for μ_{ν_μ} and μ_{ν_τ}, which are the same in our analysis. Slightly different bounds for the two moments have been found, e.g., in Refs. [18,30], where nonmaximal atmospheric mixing ($\sin^2\theta_{23} \neq 0.5$) was assumed to calculate the neutrino oscillation probability. Since we chose maximal atmospheric mixing, the expected number of events is the same for a nonzero μ_{ν_μ} or μ_{ν_τ}, hence producing the same bound. Finally, we consider the case of a single effective magnetic moment, $\mu_\nu^{\rm eff} = \mu_{\nu_e} = \mu_{\nu_\mu} = \mu_{\nu_\tau}$.

Our analysis of PandaX-4T updates the analysis of Ref. [32], where the Panda Collaboration analyzed the data from a smaller version of the current detector. In any case, due to the larger background rates observed in this experiment the bounds are always weaker than those obtained from LZ or XENONnT. It should be noted that the LZ bound obtained in our analysis is a bit weaker than those obtained in Refs. [18,30]. This is due to the more conservative use of systematic uncertainties in our analysis, since we treat each background component individually with an individual nuisance parameter. Also our XENONnT bound is slightly weaker than that from the collaboration [5] and the one from Ref. [33]. This is not worrying since we used a different statistical method and since our bound lies in any case within the XENONnT sensitivity band, see Ref. [5]. Also in the case of XENONnT, we are more conservative in the treatment of systematic uncertainties than other phenomenological analyses [30,33].

The bounds obtained from the combined analysis, which at 90% confidence level read

$$|\mu_{\nu_e}| < 10.3 \times 10^{-12}\ \mu_B, \tag{21}$$

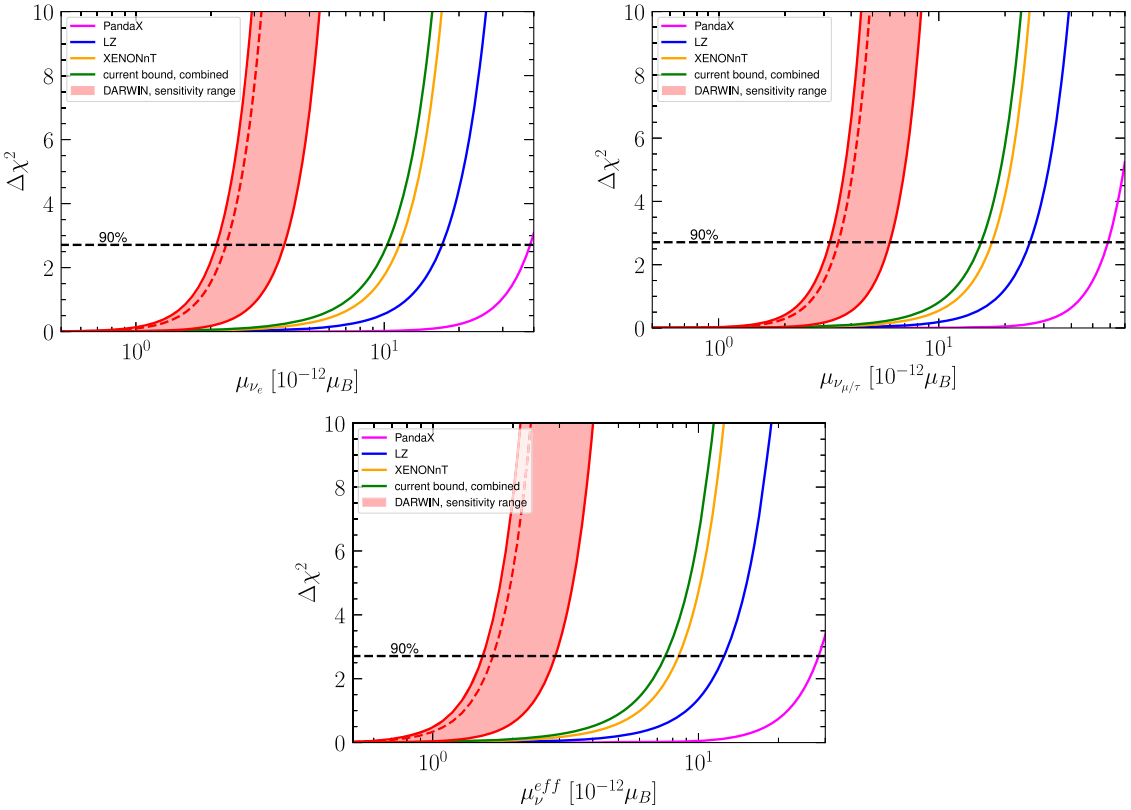

FIG. 1. $\Delta\chi^2$ profiles for the different neutrino magnetic moments obtained from the analyses of the data of PandaX (magenta), LZ (blue), XENONnT (orange) and from the combination of all experiments (green). Also shown is the sensitivity range for DARWIN (red shaded), where the worst (best) case scenario corresponds to the analysis with 30 ty (300 ty) exposure without (with) depleted ^{136}Xe background. The dashed line corresponds to 300 ty exposure without depleted ^{136}Xe background.

TABLE I. The 90% bounds ($\Delta\chi^2 = 2.71$) that can be obtained on the different neutrino magnetic moments.

Experiment	$\lvert\mu_{\nu_e}\rvert$ $[10^{-12}\mu_B]$	$\lvert\mu_{\nu_{\mu/\tau}}\rvert$ $[10^{-12}\mu_B]$	$\lvert\mu_\nu^{\rm eff}\rvert$ $[10^{-12}\mu_B]$
PandaX-4T	<38.7	<58.6	<28.3
LZ	<17.1	<25.9	<12.5
XENONnT	<11.5	<17.5	<8.4
Combined	<10.3	<15.6	<7.5
DARWIN 30 ty	<4.0	<6.0	<2.9
DARWIN 300 ty	<2.3	<3.5	<1.7
DARWIN 300 ty depleted	<2.1	<3.2	<1.5

$$|\mu_{\nu_{\mu/\tau}}| < 15.6 \times 10^{-12}\ \mu_B, \tag{22}$$

$$|\mu_\nu^{\rm eff}| < 7.5 \times 10^{-12}\ \mu_B, \tag{23}$$

are among the strongest laboratory bounds on neutrino magnetic moments [1,2,7,16]. They are about one or two orders of magnitude stronger than bounds from COHERENT or Dresden-II data [34–38], or Borexino data [39]. They are also stronger than older bounds reported in the literature [19,40–46], as the best bound on μ_{ν_e} obtained in the GEMMA experiment ($|\mu_{\nu_e}| < 2.9 \times 10^{-11}\ \mu_B$ at 90% C.L.) [19], the best bound on μ_{ν_μ} obtained in the LSND experiment ($|\mu_{\nu_\mu}| < 6.8 \times 10^{-10}\ \mu_B$ at 90% C.L.) [44], and the best bound on μ_{ν_τ} obtained in the DONUT experiment ($|\mu_{\nu_\tau}| < 3.9 \times 10^{-7}\ \mu_B$ at 90% C.L.) [45].

As also shown in Fig. 1 and Table I, these bounds can be further improved by about a factor of 2–5 by the DARWIN experiment (see also the sensitivity analysis in Ref. [47]) which would make dark matter direct detection experiments competitive with astrophysical observations, which constrain the neutrino magnetic moments below a few $10^{-12}\ \mu_B$ [48–52].

B. Neutrino millicharge

Dark matter direct detection experiments are sensitive to all of the neutrino millicharges. Note that due to the choice $\sin^2\theta_{23} = 0.5$ the bounds on the muon and tau neutrino millicharges are going to be the same for the same reason as explained in the previous section. The results from our analyses are presented in Figs. 2 and 3 and in Table II. An interesting feature can be seen in Fig. 2. While the preferred regions of the current experiments have circular shape (left panel), the region of DARWIN does not (right panel). The reason for these shapes is the following: If one substitutes Eq. (8) into Eq. (3), one sees that the cross section depends on terms which are proportional to q_{ν_α} and to $q^2_{\nu_\alpha}$. In the case of $q_{\nu_{\mu/\tau}}$, the dominating new physics contribution to the cross section comes always from the terms which are proportional to $q^2_{\nu_{\mu/\tau}}$. Also in the case of electron neutrinos the dominating contribution comes from the terms which are proportional to $q^2_{\nu_e}$ when considering current experiments. Therefore, no cancellations can occur among the new physics parameters and the preferred regions obtain the circular shape. However, in the case of DARWIN, which is sensitive to smaller millicharges, the contributions of both terms are of similar strength for electron neutrinos. Hence, correlations can appear among the parameters, which is reflected in the shape of the allowed regions. In our analyses we have taken the possible correlations among the parameters into account.

As can be seen in Figs. 2 and 3, again the PandaX-4T bound is weaker than the one from LZ, while this one is slightly weaker than that from XENONnT. Due to the conservative approach of background treatment, our

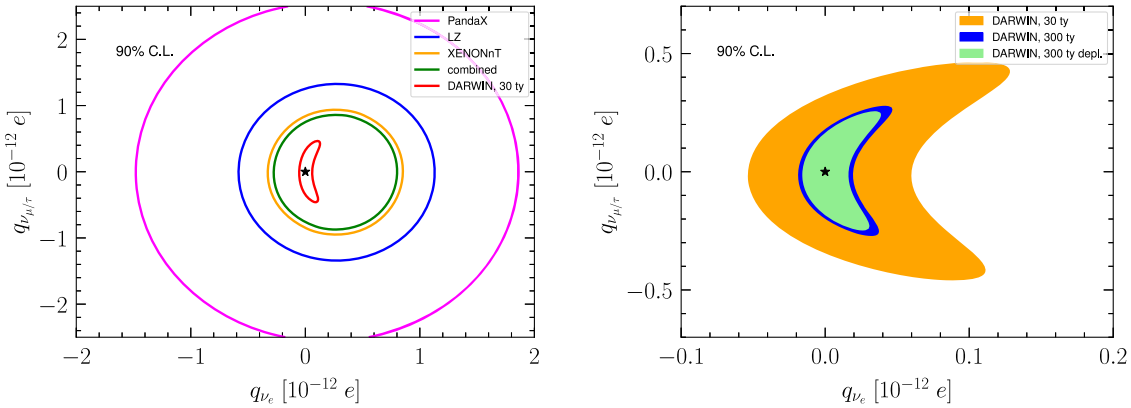

FIG. 2. Left: The 90% C.L. (2 d.o.f.) allowed regions in the $q_{\nu_e} - q_{\nu_\mu}$-plane from PandaX (magenta), LZ (blue), XENONnT (orange) and from the combination of all experiments (green) in comparison with the DARWIN sensitivity assuming 30 ty of exposure. Right: The 90% C.L. (2 d.o.f.) expected sensitivity of DARWIN for different exposures and background assumptions. The star denotes the SM value.

TABLE II. The 90% bounds ($\Delta\chi^2 = 2.71$) that can be obtained on the different neutrino millicharges.

Experiment	$q_{\nu_e}[10^{-13}e]$	$q_{\nu_\mu}[10^{-13}e]$	$\lvert q_{\nu_{e\mu/e\tau}}\rvert[10^{-13}e]$	$\lvert q_{\nu_{\mu\tau}}\rvert[10^{-13}e]$
PandaX-4T	$(-12.6, 16.4)$	$(-22.3, 22.2)$	<12.2	<15.7
LZ	$(-4.6, 9.9)$	$(-11.5, 11.3)$	<6.3	<8.1
XENONnT	$(-2.5, 7.4)$	$(-8.1, 8.0)$	<4.4	<5.7
Combined	$(-2.0, 7.0)$	$(-7.5, 7.3)$	<4.1	<5.2
DARWIN 30 ty	$(-0.4, 1.0)$	$(-4.1, 4.1)$	<2.3	<2.9
DARWIN 300 ty	$(-0.2, 0.4)$	$(-2.4, 2.5)$	<1.3	<1.7
DARWIN 300 ty depleted	$(-0.1, 0.3)$	$(-2.2, 2.3)$	<1.2	<1.6

bounds are again slightly weaker than those obtained in Refs. [18,30].

At 90% confidence level we obtain from the combined analysis:

$$q_{\nu_e} \in (-2.0, 7.0) \times 10^{-13}\ e, \tag{24}$$

$$q_{\nu_{\mu/\tau}} \in (-7.5, 7.3) \times 10^{-13}\ e, \tag{25}$$

$$|q_{\nu_{e\mu/e\tau}}| < 4.1 \times 10^{-13}\ e, \tag{26}$$

$$|q_{\nu_{\mu\tau}}| < 5.2 \times 10^{-13}\ e. \tag{27}$$

Our bound on q_{ν_e} is stronger than the bounds from the analyses of the data from TEXONO ($|q_{\nu_e}| < 1.0 \times 10^{-12}\ e$ at 90% C.L.) [41,53–55] or GEMMA ($|q_{\nu_e}| < 1.5 \times 10^{-12}\ e$ at 90% C.L.) [19,56]. Regarding $q_{\nu_{\mu/\tau}}$, the bound is more than one order of magnitude more stringent than that obtained from solar neutrinos by the XMASS Collaboration ($|q_{\nu_{\mu/\tau}}| < 1.1 \times 10^{-11}\ e$ at 90% C.L.) [57]. In the case of the nondiagonal millicharges, we improve the DRESDEN-II CEνNS bound [34] on $|q_{\nu_{e\mu/e\tau}}|$ by more than one order of magnitude and we improve the CEνNS COHERENT bound [34] on $|q_{\nu_{\mu\tau}}|$ by about three orders of magnitude.

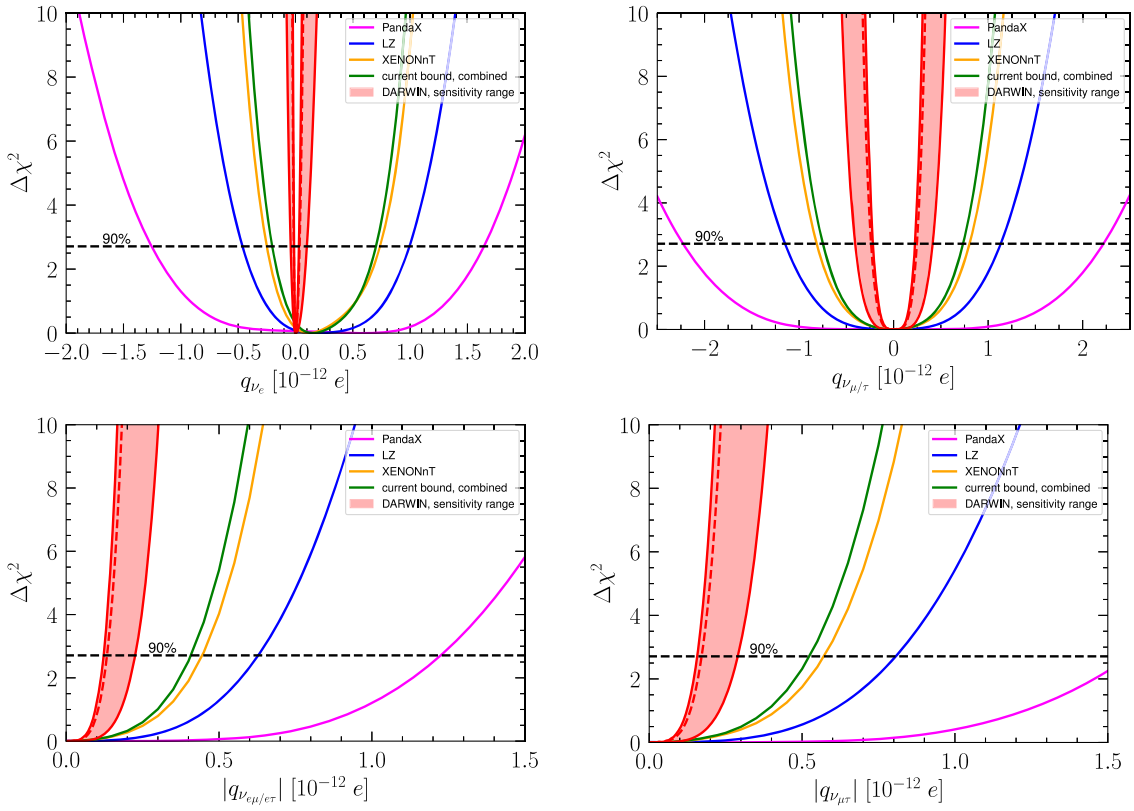

FIG. 3. $\Delta\chi^2$ profiles for the different neutrino millicharges obtained from the analysis of data of PandaX (magenta), LZ (blue), XENONnT (orange) and from the combination of all experiments (green). Also shown is the sensitivity range for DARWIN (red shaded), where the worst-(best-)case scenario corresponds to the analysis with 30 ty (300 ty) exposure without (with) depleted ^{136}Xe background. The dashed line corresponds to 300 ty exposure without depleted ^{136}Xe background.

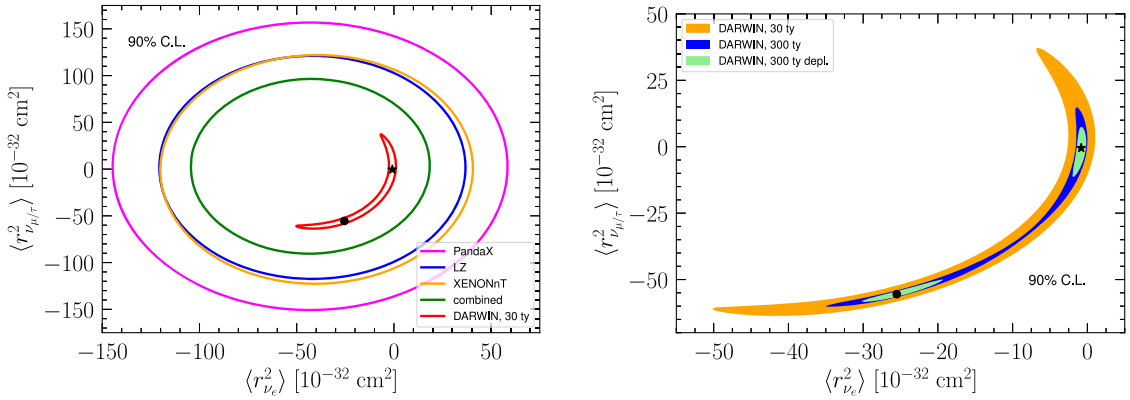

FIG. 4. Left: The 90% C.L. (2 d.o.f.) allowed regions in the $\langle r^2_{\nu_e}\rangle - \langle r^2_{\nu_\mu}\rangle$-plane from PandaX (magenta), LZ (blue), XENONnT (orange) and from the combination of all experiments (green) in comparison with the DARWIN sensitivity assuming 30 ty of exposure. Right: The 90% C.L. (2 d.o.f.) expected sensitivity of DARWIN in the $\langle r^2_{\nu_e}\rangle - \langle r^2_{\nu_\mu}\rangle$-plane for different exposures and background assumptions. The star denotes the SM value, while the black circle denotes the position of a secondary minimum found in the analysis.

All of these bounds will be further improved significantly by the DARWIN experiment, up to a factor of more than 20 in the most optimistic scenario in the case of q_{ν_e}, making dark matter direct detection experiments again competitive with astrophysical observations which constrain the neutrino millicharges below a few 10^{-14} e [58].

C. Neutrino charge radius

Finally, we can use the data to place bounds on the neutrino charge radii. Regarding the charge radii, similar correlations as discussed in the context of millicharges have to be taken into account, as can be seen in Fig. 4.

The results of the analyses of PandaX-4T, LZ and XENONnT and from the combined analysis are shown in Table III, in the left panels of Figs. 4 and 5 for the diagonal charge radii, and Fig. 6 for the nondiagonal ones. As can be seen in Table III, the bound on $\langle r^2_{\nu_e}\rangle$ is stronger than that on $\langle r^2_{\nu_{\mu/\tau}}\rangle$. Unfortunately, current dark matter direct detection experiments are not competitive with the bounds from other experiments [34,42,59] for neither of the two charge radii and they are far from the Standard Model values in Eqs. (11)–(13). Also the bounds on the nondiagonal parameters are weaker than those obtained in CEνNS experiments [34].

However, we have found that DARWIN will improve significantly the allowed region of parameter space. In the left panel of Fig. 4 we show the expected allowed region from DARWIN for a 30 ty exposure. As can be seen, DARWIN could significantly reduce the volume of the allowed parameter space. With this relatively small exposure it would be possible to set the strongest upper limit on $\langle r^2_{\nu_e}\rangle$, although the lower limit would remain weaker than the most stringent current bound obtained in the TEXONO experiment [$\langle r^2_{\nu_e}\rangle \in (-4.2, 6.6) \times 10^{-32}$ cm^2 at 90% C.L.] [59]. The size of the sensitivity region shrinks when considering a larger exposure or the better background model, as shown in the right panel of Fig. 4. In the analysis with a 300 ty exposure, values around $\langle r^2_{\nu_e}\rangle \approx -10 \times 10^{-32}\,\text{cm}^2$ and $\langle r^2_{\nu_{\mu/\tau}}\rangle \approx -35 \times 10^{-32}$ cm^2 become more disfavored, but there is still a secondary minimum present, as can be seen in the right panels of Figs. 4 and 5. The secondary solution remains even when considering the better background model. The bounds that could be obtained at 90% confidence level are

TABLE III. The 90% bounds ($\Delta\chi^2 = 2.71$) that can be obtained on the different neutrino charge radii.

Experiment	$\langle r^2_{\nu_e}\rangle[10^{-32}]$ cm^2	$\langle r^2_{\nu_{\mu/\tau}}\rangle[10^{-32}]$ cm^2	$\lvert\langle r^2_{\nu_{e\mu/e\tau}}\rangle\rvert[10^{-32}]$ cm^2	$\lvert\langle r^2_{\nu_{\mu\tau}}\rangle\rvert[10^{-32}]$ cm^2
PandaX-4T	$(-134.5, 48.2)$	$(-135.3, 141.3)$	<76.2	<97.8
LZ	$(-110.4, 26.4)$	$(-101.8, 105.5)$	<57.1	<73.3
XENONnT	$(-113.7, 34.1)$	$(-112.9, 112.3)$	<62.2	<79.9
Combined	$(-99.5, 12.8)$	$(-82.2, 88.7)$	<47.3	<60.7
DARWIN 30 ty	$(-45.3, 0.6)$	$(-62.9, 30.4)$	<28.6	<37.9
DARWIN 300 ty	$(-32.9, -14.8)$ & $(-3.6, -0.2)$	$(-59.5, -44.6)$ and $(-19.9, 11.7)$	<28.6	<37.9
DARWIN 300 ty depleted	$(-29.1, -20.7)$ &$(-1.6, -0.3)$	$(-57.8, -51.4)$ & $(-8.6, 5.7)$	<12.0	<15.7

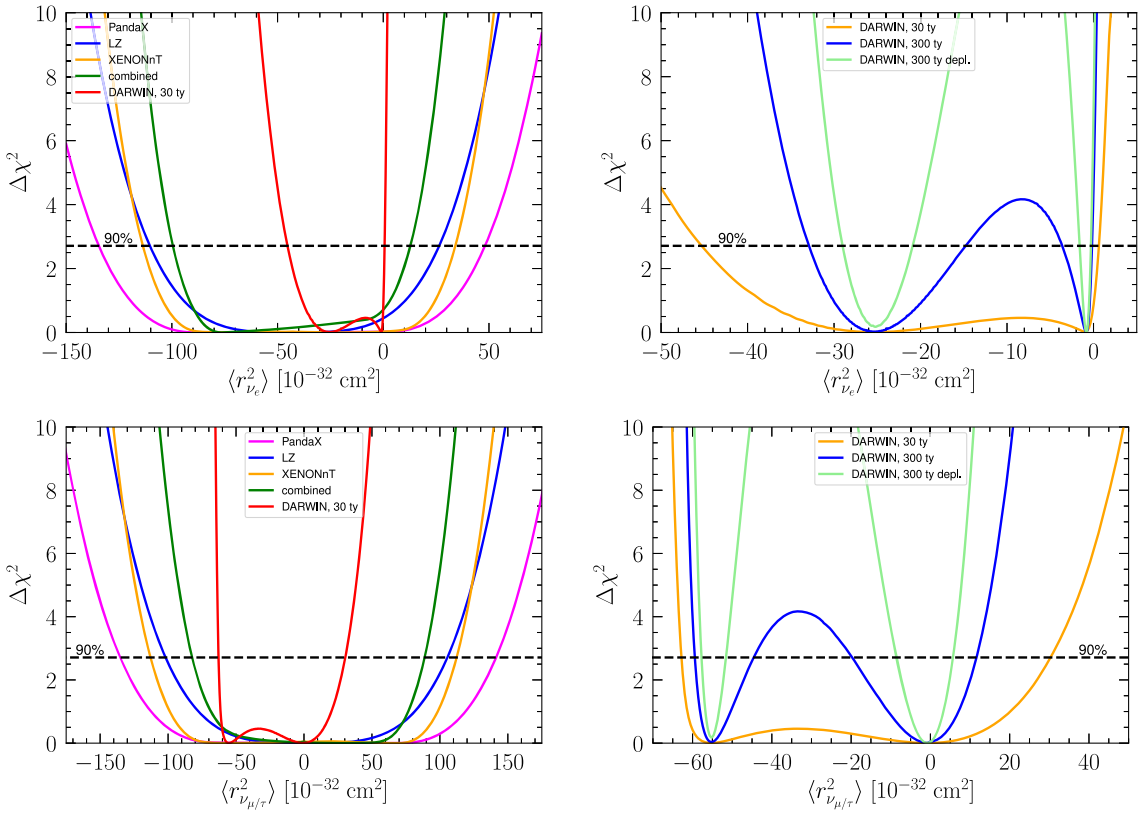

FIG. 5. $\Delta\chi^2$ profiles for the diagonal charge radii obtained from the analyses of current data (left panels) and the DARWIN sensitivity (right panels). For comparison, we also show in the left panels the DARWIN-sensitivity corresponding to an exposure of 30 ty.

$$\langle r^2_{\nu_e}\rangle \in (-45.3, 0.6)\times 10^{-32}\,\mathrm{cm}^2, \quad \text{DARWIN 30 ty}, \tag{28}$$

$$\langle r^2_{\nu_e}\rangle \in \{(-32.9, -14.8)\ \&\ (-3.6, -0.2)\}\times 10^{-32}\ \mathrm{cm}^2, \quad \text{DARWIN 300 ty}, \tag{29}$$

$$\langle r^2_{\nu_e}\rangle \in \{(-29.1, -20.7)\ \&\ (-1.6, -0.3)\}\times 10^{-32}\ \mathrm{cm}^2, \quad \text{DARWIN 300 ty, depleted}. \tag{30}$$

Thus, DARWIN 300 ty could improve the current best limit on $\langle r^2_{\nu_e}\rangle$ obtained in the TEXONO experiment ($\langle r^2\rangle_{\nu_e} \in (-4.2, 6.6)\times 10^{-32}$ at 90% C.L.) [59] (taking into account that the secondary solution is excluded by TEXONO and other bounds; see, e.g., Refs. [1,2,7,16]) and could indicate that $\langle r^2_{\nu_e}\rangle$ is negative. This would be the first indication of a nonzero value of a neutrino charge radius, in agreement with the Standard Model prediction (11).

In the lower panels of Fig. 5 we show the sensitivity of DARWIN to the charge radius $\langle r^2_{\nu_\mu}\rangle$. Although not as strong as for $\langle r^2_{\nu_e}\rangle$, DARWIN could provide strong bounds on this quantity, which read at 90% confidence level

$$\langle r^2_{\nu_\mu}\rangle \in (-62.9, 30.4)\times 10^{-32}\,\mathrm{cm}^2, \quad \text{DARWIN 30 ty}, \tag{31}$$

$$\langle r^2_{\nu_\mu}\rangle \in \{(-59.5, -44.6)\ \&\ (-19.9, 11.7)\}\times 10^{-32}\ \mathrm{cm}^2, \quad \text{DARWIN 300 ty}, \tag{32}$$

$$\langle r^2_{\nu_\mu}\rangle \in \{(-57.8, -51.4)\ \&\ (-8.6, 5.7)\}\times 10^{-32}\ \mathrm{cm}^2, \quad \text{DARWIN 300 ty, depleted}. \tag{33}$$

Such bounds would be complementary to the bounds obtained in other experiments [34,42,60,61]. Note that the secondary minimum obtained in our DARWIN analyses requires both charge radii to be different from the Standard Model values. We could eliminate the secondary minimum by using external constraints on $\langle r^2_{\nu_e}\rangle$ (e.g the TEXONO bound [59]) or $\langle r^2_{\nu_\mu}\rangle$ (e.g. the one from Ref. [42]).

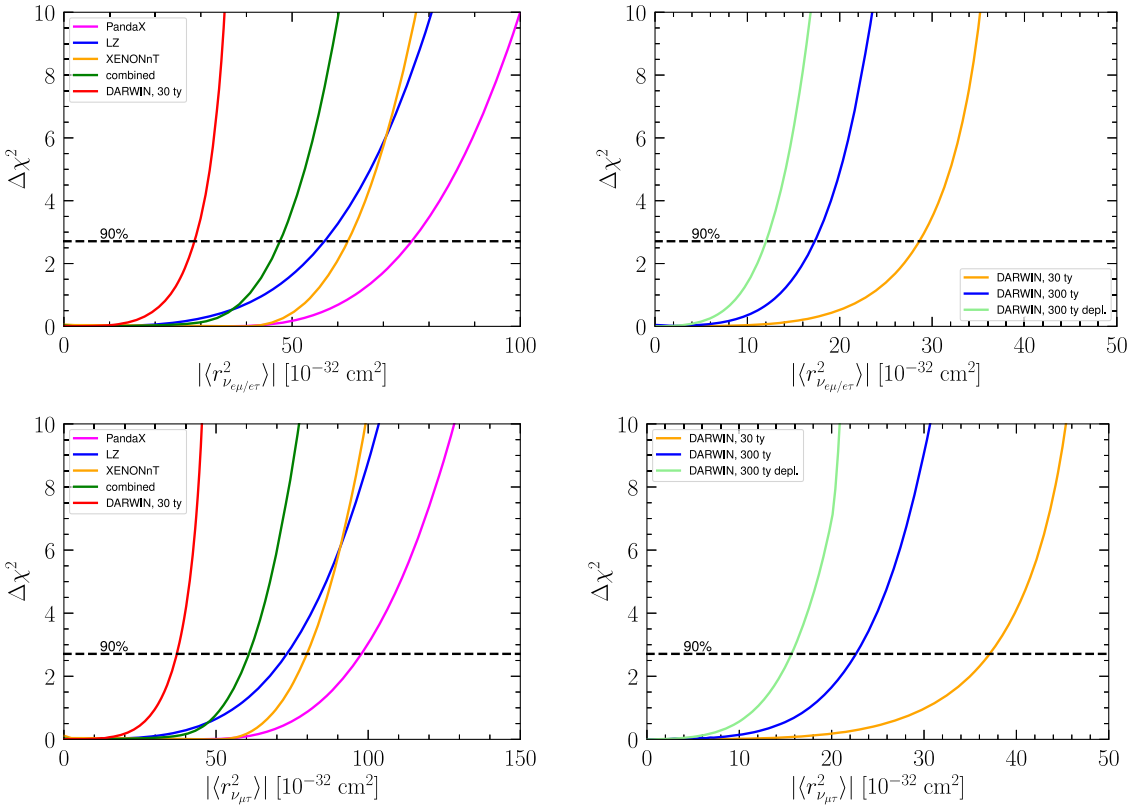

FIG. 6. $\Delta\chi^2$ profiles for the nondiagonal charge radii obtained from the analyses of current data (left panels) and the DARWIN sensitivity (right panels). For comparison, we also show in the left panels the DARWIN-sensitivity corresponding to an exposure of 30 ty.

Regarding the transition charge radii, the DARWIN sensitivity is shown in comparison with the current bounds in Fig. 6 and in the last two columns of Table III. In this case the bounds that DARWIN could set assuming an exposure of 30 ty are similar in strength to those obtained with CEνNS in Ref. [34]. Only with a larger exposure and a better background model the current bounds could be improved by a factor of about 2–3.

V. CONCLUSIONS

In this paper we have analyzed the electron recoil data from the dark matter direct detection experiments PandaX-4T, LZ and XENONnT to place constraints on neutrino electromagnetic properties. We also explored the sensitivity of the future experiment DARWIN. We implemented a more realistic treatment of systematic uncertainties than in other phenomenological analyses previously performed in the literature, following closer what is done by the collaborations.

We have set strong limits on the neutrino magnetic moments and on the neutrino millicharges. These are still weaker than those from astrophysical probes. However, we have shown that the next generation experiment DARWIN will put the sensitivity of dark matter direct detection experiments into the same ballpark.

We have shown that in the case of the neutrino charge radii current dark matter direct detection experiments are not competitive with other types of experiments. However, this situation will change dramatically for DARWIN. Under ideal circumstances a measurement of $\langle r^2_{\nu_e}\rangle$ could be possible for the first time.

An interesting feature of dark matter direct detection experiments which can detect solar neutrinos is that part of the neutrinos arrives as ν_τ, hence allowing us to set bounds also on the ν_τ related quantities, which is not possible with other experiments.

Summarizing, we have shown that current and particularly future dark matter direct detection experiments provide a powerful tool to test neutrino electromagnetic properties.

ACKNOWLEDGMENTS

We are very thankful to Dimitris Papoulias for helful discussions. C. G. and C. A. T. acknowledge support from *Departments of Excellence* grant awarded by MIUR and the research grant *TAsP (Theoretical Astroparticle Physics)* funded by Istituto Nazionale di Fisica Nucleare (INFN).

[1] C. Giunti and A. Studenikin, Neutrino electromagnetic interactions: A window to new physics, Rev. Mod. Phys. **87**, 531 (2015).

[2] C. Giunti, K. A. Kouzakov, Y.-F. Li, A. V. Lokhov, A. I. Studenikin, and S. Zhou, Electromagnetic neutrinos in laboratory experiments and astrophysics, Ann. Phys. (Amsterdam) **528**, 198 (2016).

[3] D. Zhang *et al.* (PandaX Collaboration), Search for light fermionic dark matter absorption on electrons in PandaX-4T, Phys. Rev. Lett. **129**, 161804 (2022).

[4] J. Aalbers *et al.* (LZ Collaboration), First dark matter search results from the LUX-ZEPLIN (LZ) experiment, Phys. Rev. Lett. **131**, 041002 (2023).

[5] E. Aprile *et al.* (XENON Collaboration), Search for new physics in electronic recoil data from XENONnT, Phys. Rev. Lett. **129**, 161805 (2022).

[6] J. Aalbers *et al.* (DARWIN Collaboration), Solar neutrino detection sensitivity in DARWIN via electron scattering, Eur. Phys. J. C **80**, 1133 (2020).

[7] C. Giunti, J. Gruszko, B. Jones, L. Kaufman, D. Parno, and A. Pocar, Report of the topical group on neutrino properties for snowmass 2021, arXiv:2209.03340.

[8] J. Bahcall, http://www.sns.ias.edu/~jnb/SNdata/sndata.html.

[9] J. N. Bahcall and R. K. Ulrich, Solar models, neutrino experiments and helioseismology, Rev. Mod. Phys. **60**, 297 (1988).

[10] J. N. Bahcall, The ^{7}Be solar neutrino line: A reflection of the central temperature distribution of the sun, Phys. Rev. D **49**, 3923 (1994).

[11] J. N. Bahcall, E. Lisi, D. E. Alburger, L. De Braeckeleer, S. J. Freedman, and J. Napolitano, Standard neutrino spectrum from ^{8}B decay, Phys. Rev. C **54**, 411 (1996).

[12] F. L. Villante and A. Serenelli, The relevance of nuclear reactions for standard solar models construction, Front. Astron. Space Sci. **7**, 112 (2021).

[13] P. F. de Salas, D. V. Forero, S. Gariazzo, P. Martinez-Mirave, O. Mena, C. A. Ternes, M. Tortola, and J. W. F. Valle, 2020 Global reassessment of the neutrino oscillation picture, J. High Energy Phys. 02 (2020) 071.

[14] I. Esteban, M. C. Gonzalez-Garcia, M. Maltoni, T. Schwetz, and A. Zhou, The fate of hints: Updated global analysis of three-flavor neutrino oscillations, J. High Energy Phys. 09 (2020) 178.

[15] F. Capozzi, E. Di Valentino, E. Lisi, A. Marrone, A. Melchiorri, and A. Palazzo, The unfinished fabric of the three neutrino paradigm, Phys. Rev. D **104**, 083031 (2021).

[16] R. L. Workman (Particle Data Group), Review of particle physics, Prog. Theor. Exp. Phys. **2022**, 083C01 (2022).

[17] S. A. Fayans, L. A. Mikaelyan, and V. V. Sinev, Weak and magnetic inelastic scattering of anti-neutrinos on atomic electrons, Phys. At. Nucl. **64**, 1475 (2001).

[18] M. Atzori Corona, W. M. Bonivento, M. Cadeddu, N. Cargioli, and F. Dordei, New constraint on neutrino magnetic moment and neutrino millicharge from LUX-ZEPLIN dark matter search results, Phys. Rev. D **107**, 053001 (2023).

[19] A. G. Beda, V. B. Brudanin, V. G. Egorov, D. V. Medvedev, V. S. Pogosov, M. V. Shirchenko, and A. S. Starostin, The results of search for the neutrino magnetic moment in GEMMA experiment, Adv. High Energy Phys. **2012**, 350150 (2012).

[20] K. Fujikawa and R. Shrock, The magnetic moment of a massive neutrino and neutrino spin rotation, Phys. Rev. Lett. **45**, 963 (1980).

[21] P. B. Pal and L. Wolfenstein, Radiative decays of massive neutrinos, Phys. Rev. D **25**, 766 (1982).

[22] R. E. Shrock, Electromagnetic properties and decays of Dirac and Majorana neutrinos in a general class of gauge theories, Nucl. Phys. **B206**, 359 (1982).

[23] J. Bernabeu, L. G. Cabral-Rosetti, J. Papavassiliou, and J. Vidal, On the charge radius of the neutrino, Phys. Rev. D **62**, 113012 (2000).

[24] J. Bernabeu, J. Papavassiliou, and J. Vidal, On the observability of the neutrino charge radius, Phys. Rev. Lett. **89**, 101802 (2002).

[25] J. Bernabeu, J. Papavassiliou, and J. Vidal, The neutrino charge radius is a physical observable, Nucl. Phys. **B680**, 450 (2004).

[26] M. Cadeddu, C. Giunti, K. A. Kouzakov, Y. F. Li, A. I. Studenikin, and Y. Y. Zhang, Neutrino charge radii from COHERENT elastic neutrino-nucleus scattering, Phys. Rev. D **98**, 113010 (2018).

[27] M. Cadeddu, F. Dordei, C. Giunti, Y. F. Li, and Y. Y. Zhang, Neutrino, electroweak and nuclear physics from COHERENT elastic neutrino-nucleus scattering with refined quenching factor, Phys. Rev. D **101**, 033004 (2020).

[28] J. Aalbers *et al.* (LZ Collaboration), Background determination for the LUX-ZEPLIN dark matter experiment, Phys. Rev. D **108**, 012010 (2023).

[29] J. Aalbers *et al.* (LZ Collaboration), A search for new physics in low-energy electron recoils from the first LZ exposure, Phys. Rev. D **108**, 072006 (2023).

[30] S. K. A., A. Majumdar, D. K. Papoulias, H. Prajapati, and R. Srivastava, Implications of first LZ and XENONnT results: A comparative study of neutrino properties and light mediators, Phys. Lett. B **839**, 137742 (2023).

[31] E. Aprile *et al.* (XENON Collaboration), Excess electronic recoil events in XENON1T, Phys. Rev. D **102**, 072004 (2020).

[32] X. Zhou *et al.* (PandaX-II Collaboration), A search for solar axions and anomalous neutrino magnetic moment with the complete PandaX-II data, Chin. Phys. Lett. **38**, 011301 (2021); Chin. Phys. Lett. **38**, 109902(E) (2021).

[33] A. N. Khan, Light new physics and neutrino electromagnetic interactions in XENONnT, Phys. Lett. B **837**, 137650 (2023).

[34] M. Atzori Corona, M. Cadeddu, N. Cargioli, F. Dordei, C. Giunti, Y. F. Li, C. A. Ternes, and Y. Y. Zhang, Impact of the Dresden-II and COHERENT neutrino scattering data on neutrino electromagnetic properties and electroweak physics, J. High Energy Phys. 09 (2022) 164.

[35] P. Coloma, I. Esteban, M. C. Gonzalez-Garcia, L. Larizgoitia, F. Monrabal, and S. Palomares-Ruiz, Bounds on new physics with data of the Dresden-II reactor experiment and COHERENT, J. High Energy Phys. 05 (2022) 037.

[36] J. Liao, H. Liu, and D. Marfatia, Implications of the first evidence for coherent elastic scattering of reactor neutrinos, Phys. Rev. D **106**, L031702 (2022).

[37] A. N. Khan, Neutrino millicharge and other electromagnetic interactions with COHERENT-2021 data, Nucl. Phys. **B986**, 116064 (2023).
[38] V. De Romeri, O. G. Miranda, D. K. Papoulias, G. Sanchez Garcia, M. Tórtola, and J. W. F. Valle, Physics implications of a combined analysis of COHERENT CsI and LAr data, J. High Energy Phys. 04 (2023) 035.
[39] P. Coloma, P. Coloma, M. C. Gonzalez-Garcia, M. C. Gonzalez-Garcia, M. Maltoni, M. Maltoni, J. a. P. Pinheiro, J. a. P. Pinheiro, S. Urrea, and S. Urrea, Constraining new physics with Borexino Phase-II spectral data, J. High Energy Phys. 07 (2022) 138; J. High Energy Phys. 11 (2022) 138(E).
[40] Z. Daraktchieva *et al.* (MUNU Collaboration), Final results on the neutrino magnetic moment from the MUNU experiment, Phys. Lett. B **615**, 153 (2005).
[41] H. T. Wong *et al.* (TEXONO Collaboration), A search of neutrino magnetic moments with a high-purity germanium detector at the Kuo-Sheng nuclear power station, Phys. Rev. D **75**, 012001 (2007).
[42] L. A. Ahrens *et al.*, Determination of electroweak parameters from the elastic scattering of muon neutrinos and antineutrinos on electrons, Phys. Rev. D **41**, 3297 (1990).
[43] R. C. Allen *et al.*, Study of electron-neutrino electron elastic scattering at LAMPF, Phys. Rev. D **47**, 11 (1993).
[44] L. B. Auerbach *et al.* (LSND Collaboration), Measurement of electron—neutrino—electron elastic scattering, Phys. Rev. D **63**, 112001 (2001).
[45] R. Schwienhorst *et al.* (DONUT Collaboration), A new upper limit for the tau—neutrino magnetic moment, Phys. Lett. B **513**, 23 (2001).
[46] B. C. Canas, O. G. Miranda, A. Parada, M. Tortola, and J. W. F. Valle, Updating neutrino magnetic moment constraints, Phys. Lett. B **753**, 191 (2016); Phys. Lett. B **757**, 568(A) (2016).
[47] D. Aristizabal Sierra, R. Branada, O. G. Miranda, and G. Sanchez Garcia, Sensitivity of direct detection experiments to neutrino magnetic dipole moments, J. High Energy Phys. 12 (2020) 178.
[48] A. Ayala, J. C. D'Olivo, and M. Torres, Bound on the neutrino magnetic moment from chirality flip in supernovae, Phys. Rev. D **59**, 111901 (1999).
[49] N. Viaux, M. Catelan, P. B. Stetson, G. Raffelt, J. Redondo, A. A. R. Valcarce, and A. Weiss, Neutrino and axion bounds from the globular cluster M5 (NGC 5904), Phys. Rev. Lett. **111**, 231301 (2013).
[50] A. H. Córsico, L. G. Althaus, M. M. Miller Bertolami, S. O. Kepler, and E. García-Berro, Constraining the neutrino magnetic dipole moment from white dwarf pulsations, J. Cosmol. Astropart. Phys. 08 (2014) 054.
[51] F. Capozzi and G. Raffelt, Axion and neutrino bounds improved with new calibrations of the tip of the red-giant branch using geometric distance determinations, Phys. Rev. D **102**, 083007 (2020).
[52] K. Mori, M. Kusakabe, A. B. Balantekin, T. Kajino, and M. A. Famiano, Enhancement of lithium in red clump stars by the additional energy loss induced by new physics, Mon. Not. R. Astron. Soc. **503**, 2746 (2021).
[53] H. B. Li *et al.* (TEXONO Collaboration), Limit on the electron neutrino magnetic moment from the Kuo-Sheng reactor neutrino experiment, Phys. Rev. Lett. **90**, 131802 (2003).
[54] S. N. Gninenko, N. V. Krasnikov, and A. Rubbia, Search for millicharged particles in reactor neutrino experiments: A probe of the PVLAS anomaly, Phys. Rev. D **75**, 075014 (2007).
[55] J.-W. Chen, H.-C. Chi, H.-B. Li, C. P. Liu, L. Singh, H. T. Wong, C.-L. Wu, and C.-P. Wu, Constraints on millicharged neutrinos via analysis of data from atomic ionizations with germanium detectors at sub-keV sensitivities, Phys. Rev. D **90**, 011301 (2014).
[56] A. Studenikin, New bounds on neutrino electric millicharge from limits on neutrino magnetic moment, Europhys. Lett. **107**, 21001 (2014); Europhys. Lett. **107**, 39901(E) (2014).
[57] K. Abe *et al.* (XMASS Collaboration), Search for exotic neutrino-electron interactions using solar neutrinos in XMASS-I, Phys. Lett. B **809**, 135741 (2020).
[58] G. G. Raffelt, Limits on neutrino electromagnetic properties: An update, Phys. Rep. **320**, 319 (1999).
[59] M. Deniz *et al.* (TEXONO Collaboration), Measurement of Nu(e)-bar -electron scattering cross-section with a CsI(Tl) scintillating crystal array at the Kuo-Sheng nuclear power reactor, Phys. Rev. D **81**, 072001 (2010).
[60] P. Vilain *et al.* (CHARM-II Collaboration), Experimental study of electromagnetic properties of the muon-neutrino in neutrino—electron scattering, Phys. Lett. B **345**, 115 (1995).
[61] A. N. Khan, $\sin^2\theta_W$ estimate and neutrino electromagnetic properties from low-energy solar data, J. Phys. G **46**, 035005 (2019).